

Computational Modeling and Analysis of Aeroelastic Wing Flutter

Karthik Menon¹ and Rajat Mittal²
Johns Hopkins University, Baltimore, MD 21218

This paper reports on simulations of flow-induced aeroelastic pitching of an airfoil. Incompressible, viscous flow over a modified NACA0015 airfoil is coupled with a two degree-of-freedom model of an elastically supported airfoil and we examine the response as a function of spring stiffness, equilibrium angle-of-attack, as well as location of the elastic axis. We also highlight some features of the associated flow and vortex wake patterns. Finally, we report on the application of a novel force partitioning method that enables us to dissect the contribution of the various vortices and other mechanisms on the aerodynamic forces experienced by the fluttering airfoil.

I. Introduction

Investigations of unsteady aerodynamics in the context of dynamic stall and stall flutter pitching airfoils have been carried out for a number of years (Ericsson & Reding [1], McCroskey [2]). Numerous studies have reported on the large-scale separation and reattachment over the suction surface of dynamically pitching airfoils, as well as on the strong influence of large vortex structures shed off the leading edge for this configuration. More recently, Lee and Gerontakos [3] carried out an extensive study of the separation, reattachment, and transition of the flow over the surface of a sinusoidally oscillating airfoil. They point to the significant effect of the leading-edge vortex on the unsteady dynamics as well as its effect on the delay of separation and stall of a pitching airfoil. Other studies have focused on the effect of parameters such as oscillation frequency and amplitude on the onset of dynamic stall (Amiralaee et al. [4], Lind & Jones [5], Young & Lai [6]), and have found that the oscillation frequency plays a crucial role in the onset of dynamic stall. In another study, Bhat & Govardhan [7] used a sinusoidally oscillating airfoil, along with calculations of energy transfer over a cycle, to map out flutter boundaries as a function of oscillation frequency and amplitude.

Most of these aforementioned studies, have primarily utilized prescribed oscillations as a tool to understand these unsteady effects and there are far fewer studies involving flow-induced, or free oscillations. While prescribed flutter provides some insights about the fluid dynamics of aeroelastically fluttering airfoils, it misses many features that are introduced by the two-way coupling between the flow and the foil. Dimitriadis and Lee [8] carried out a study of an airfoil with pitch and heave degrees of freedom, and showed the occurrence of various bifurcations in the dynamical response of the system. Further, they were able to classify these bifurcations and examine the mechanism behind the observed stall flutter during these different regimes. In another study of flow-induced oscillations, Ducoin et al. [9] used a combination of experimental data and quasi-steady numerical simulations to analyze the stability of a flexible hydrofoil and attributed the onset of the pitch-up instability (and consequently, the tendency to reach static divergence) to the upstream location of the center-of-pressure with respect to the elastic axis. They also showed that viscous effects during stall cause the center-of-pressure to move downstream towards the elastic axis, thus delaying static divergence. While the work of Dimitriadis and Lee employed experiments, a number of earlier studies have investigated flow-induced oscillations in airfoils and flat plates using simplified and low-order numerical techniques (Dowell [10], Holmes & Marsden [11], Jumper et al. [12]). However, high fidelity computational modeling is not so common, likely due to the computational expense and complexity.

Here, we use high-fidelity flow simulations to model the flow-induced pitching oscillations of an airfoil at $Re = 1000$. In order to establish a baseline for the analysis of the flow-induced flutter of the airfoil, we also report on static airfoil characteristics at this low Reynolds number. As mentioned before, due to the fact that very little data currently

¹ Graduate Student, Department of Mechanical Engineering (kmenon@jhu.edu).

² Professor, Department of Mechanical Engineering (mittal@jhu.edu), AIAA Associate Fellow.

exists for flow-induced oscillations at these Reynolds numbers, we aim to provide some preliminary insight into the system using broad parametric sweeps of elastic stiffness, equilibrium angle-of-attack, and hinge location for pitching oscillations. The primary aim of this parametric survey is to use this initial understanding of the system to inform more detailed investigations of aeroelastic wing flutter.

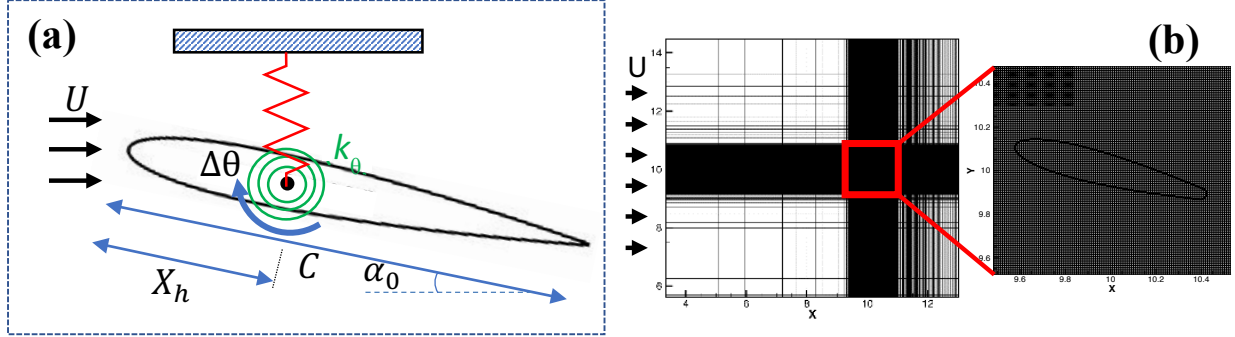


Figure 1. (a) Schematic of the aeroelastic model; (b) Computational setup

II. Modeling and Simulation Methodology

A. Problem Description

Our model (see Figure 1) consists of a NACA0015 airfoil, with the trailing-edge rounded at 87% chord to alleviate resolution requirements. This airfoil is attached to linear springs corresponding to each degree of freedom, i.e., a tension/compression spring in the heave direction and a torsion spring for pitching oscillations. In this paper, the focus is on pitch oscillations, and consequently, the tension/compression spring is “locked” and only angular motion is allowed to take place. The torsion spring has spring and damping constants given by k_θ and ζ_θ respectively, which are important parameters in the dynamical response of the system. Furthermore, the location along the chord at which the body is hinged, i.e. the elastic axis, is denoted by X_h . This is another parameter that is explored in this study. This system is immersed in an incompressible fluid with freestream velocity given by U_∞ and the fluid is governed by the incompressible Navier-Stokes equations.

The dynamical equation for the rigid-body system described above is:

$$\left(\frac{2I}{\rho C^4}\right)\ddot{\theta} + \left(\frac{2\zeta_\theta}{\rho U_\infty C^3}\right)\dot{\theta} + \left(\frac{2k_\theta}{\rho U_\infty^2 C^2}\right)(\theta - \alpha_0) = C_M$$

where I is the moment of inertia of the body, ρ is the fluid density, C is the chord length, and α and α_0 are respectively the instantaneous and equilibrium angles of attack respectively. The dynamical equation is scaled by the fluid quantities to simplify the interfacing between the solid and fluid solvers, This leads to nondimensional numbers representing the scaled moment of inertia, $I^* = \left(\frac{2I}{\rho C^4}\right)$, mechanical damping, $b_\theta^* = \left(\frac{2\zeta_\theta}{\rho U_\infty C^3}\right)$, and spring constant, $k_\theta^* = \left(\frac{2k_\theta}{\rho U_\infty^2 C^2}\right)$ on the left-hand side of the above equation, and the forcing term on the right-hand side taking the form of the coefficient of moment, $C_M = \left(\frac{2M}{\rho U_\infty^2 C^2}\right)$. We also introduce a small damping (15% of the critical damping) which mimics frictional losses in the torsional system, hence we set $b_\theta^* = 0.3\sqrt{k_\theta^* I^*}$, where the moment of inertia used is $I^* = 2.07$. To be consistent with existing literature on flow-induced vibrations, we present our results in terms of a reduced velocity, $U^* = U_\infty/f_n C$, where f_n is the natural frequency of the torsion spring related to the the above parameters as $f_n = \frac{1}{2\pi}\sqrt{\frac{k_\theta}{I}}$. Finally, the Reynolds number in this study, defined as $Re = U_\infty C/\nu$, is fixed at $Re = 1000$.

B. Computational Method

We simulate the coupled fluid-structure system using the immersed boundary method code ViCar3D developed by Mittal et. al. [13,14], which allows us to preserve sharp interfaces along the surface of our geometry using a non-conformal Cartesian grid. This is particularly valuable in fluid-structure interaction studies as it allows us to simulate a large variety of shapes as well as response motions without having to regenerate body conformal grid for the moving foil. The incompressible flow equations are solved using a projection technique, and the pressure Poisson equation is solved using the geometric multigrid method. Second-order finite differences are used for all spatial derivatives, and time integration is performed using a second order Adams-Bashforth method for the non-linear term. The fluid-structure coupling is carried out by using Lagrangian marker points on the surface of the solid body, where forcing quantities are calculated and passed on to the solid dynamical equation (Equation 1) explicitly using the forward-Euler method. The foil is immersed in a domain of size $18C \times 20C$, and the grid resolution around the solid body provides about 125 points along the chord.

III. Results and Discussion

In presenting our results, we begin with a discussion of static airfoils at the Reynolds number of 1000, which matches the regime for which the aeroelastic flutter simulations are conducted. This data is meant to aid our subsequent analysis of the aeroelastically pitching foil. We then discuss pitching airfoils and focus on three key parameters: the reduced velocity, the equilibrium angle-of-attack, and the location of the hinge point. As mentioned previously, this is a small region of the vast parameter space that governs this problem. Nevertheless these results provide some interesting insight into the dynamics of pitching airfoils, and a starting point for subsequent work on understanding the physics of aeroelastic flutter. Finally, we present a novel force decomposition method, which could serve as a useful tool in the analysis of fluid-structure interaction problems, and we discuss this in the context of wing-flutter.

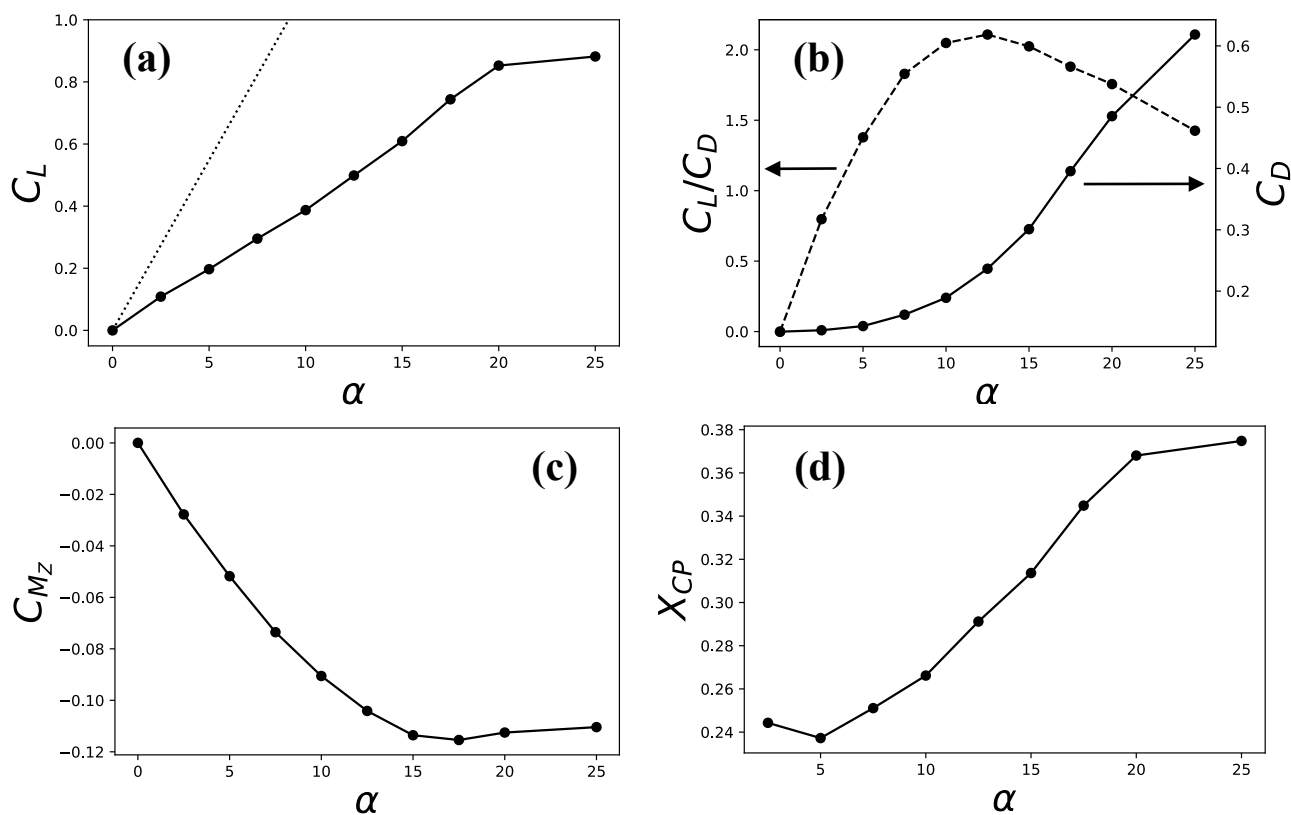


Figure 2. Aerodynamic quantities for a static airfoil at $Re = 1000$: (a) Coefficient of lift (dotted line indicates 2π slope); (b) Coefficient of drag and lift-to-drag ratio ; (c) Coefficient of moment about mid-chord; (d) Location of center-of-pressure X_{CP} , shown as a fraction of chord length.

A. Static Airfoil Performance

The current study focuses on the dynamical behaviour of aeroelastically pitching airfoils at $Re = 1000$. The flow at this Reynolds number can be resolved well and the computational requirements at this Reynolds number allow us to conduct a large parameter survey of this configuration. Figure 2(a) shows the lift curve for the truncated NACA0015 airfoil used in this study. It is observed that the slope of the curve is lower than the 2π slope that is predicted by thin-airfoil theory. Tests indicate that the aerodynamic performance of the airfoil is mostly unaffected by the rounding of the trailing-edge at 87% chord. It is also noted that the static stall occurs around 20° . Some flow visualizations from these static airfoil simulations are shown in Figure 3, with the corresponding angles of attack marked on the $C_L - \alpha$ curve. It is seen that there is some flow separation at $\alpha = 15^\circ$, but the flow over the suction surface is completely separated at $\alpha = 25^\circ$. The corresponding coefficient of drag and the lift-to-drag ratio are plotted in Figure 2(b). As expected, increasing angle-of-attack leads to increasing drag, and the onset of flow separation above $\alpha = 10^\circ$ causes a large increase in the drag coefficient. The coefficient of pitching moment, calculated about the mid-chord, is shown in Figure 2(c) where pitch-down moment is defined as positive. We see that the magnitude of pitching moment increases with increasing angle-of-attack until the airfoil stalls. In Figure 2(d), we plot the location of center-of-pressure, which is an important parameter in determining the stability of the system to angular perturbations. It is interesting to note that the center-of-pressure initially moves upstream and subsequently moves downstream for increasing angle-of-attack – moving from about quarter-chord to roughly $0.37C$ at stall. We will see that this plays an important role in the pitching response of the system, and the choice of X_h used.

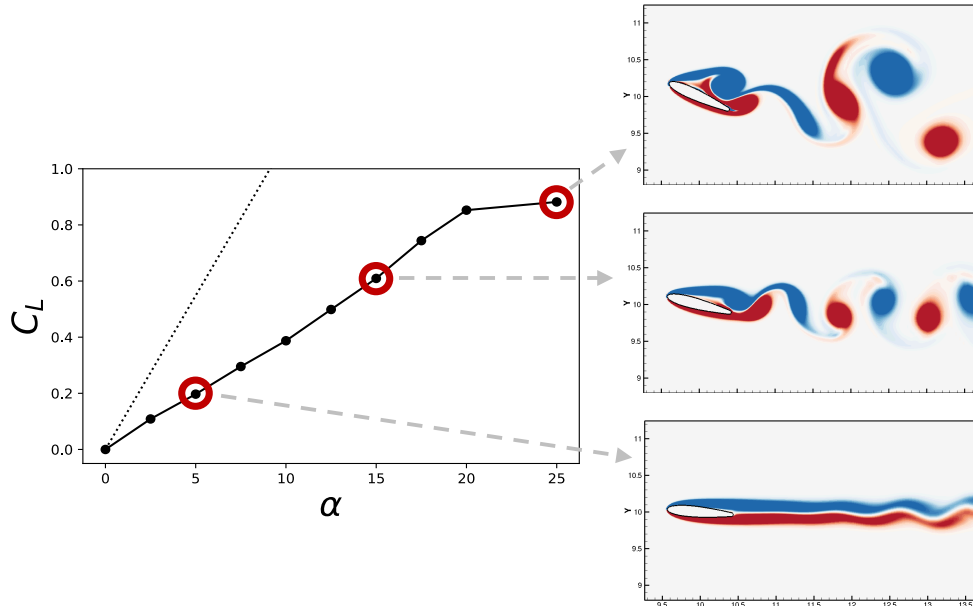


Figure 3. Flow visualizations for a static airfoil at $\alpha_0 = 5^\circ, 15^\circ, 25^\circ$

B. Effect of Reduced Velocity

As defined previously, the reduced velocity U^* is the ratio of the time-scale associated with the natural frequency of the torsion spring to the convective time-scale. This ratio is considered an important parameter in flow-induced vibrations. For these simulations the system is initialized with a zero angular displacement and zero angular velocity and the simulations are run until the system reaches a stationary state.

We begin with a qualitative analysis of the flow field around the pitching airfoil, shown in Figure 4 for two cases with $\alpha_0 = 15^\circ$. Each panel of figures shows roughly equally-spaced snapshots of the system over one pitch up-pitch down cycle. On the left-hand side panel we show data from a case with $U^* = 4.6$. This is compared with results from a case with $U^* = 7.3$, shown on the right-hand side panel. These cases show a maximum pitch deflection of roughly 20° and 60° respectively. We see in Figures 4(i)-(iv) that both of these cases produce fairly complicated vortex shedding patterns downstream of the airfoil. Also, both cases show the generation and shedding of a large leading-

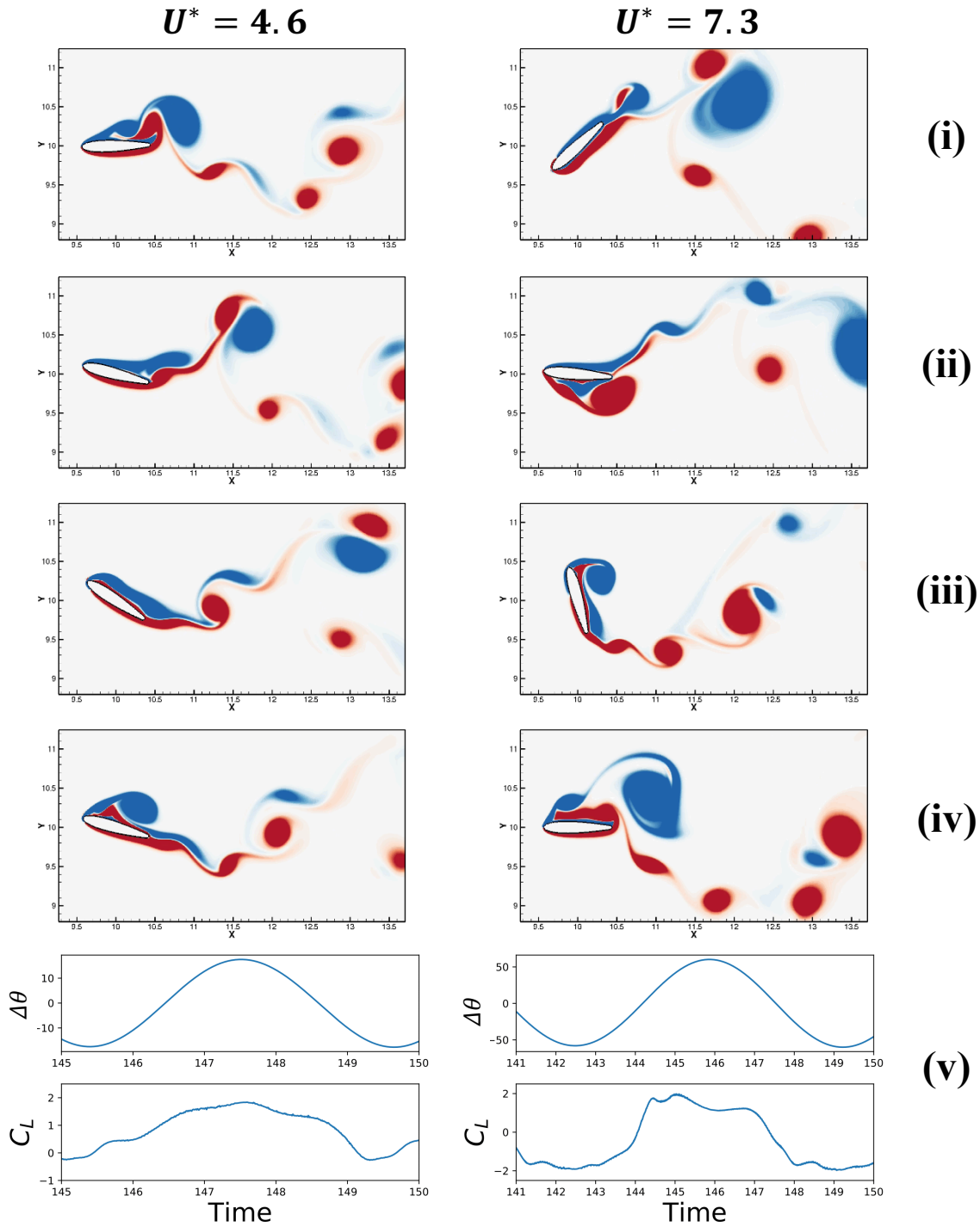


Figure 4. (i)-(iv) Flow visualization snapshots over one period of oscillation; (v) Timeseries of pitch angle (degrees) and C_L corresponding to the same oscillation period; for two cases with $\alpha_0 = 15^\circ$, and $U^* = 4.6$ (left panel) and $U^* = 7.3$ (right panel).

edge vortex during the downward stroke of the pitching cycle. This has been reported in previous studies of forced pitching oscillations in airfoils. However, from a comparison of the flow fields in Figures 4(ii) and 4(iv) it is evident that the case with $U^* = 4.6$ sheds one LEV per cycle, during the downward stroke, whereas the case with $U^* = 7.3$ sheds 2 LEVs of different intensities during each half-stroke of the cycle, and these are shed from the top and bottom

of the symmetric airfoil. This produces a double-peaked C_L variation over the oscillation cycle, shown in Figure 4(v), which is absent (or not as strong) in the case of $U^* = 4.6$. As expected, these vortices have a large effect on the variation of C_M over a cycle (not shown here).

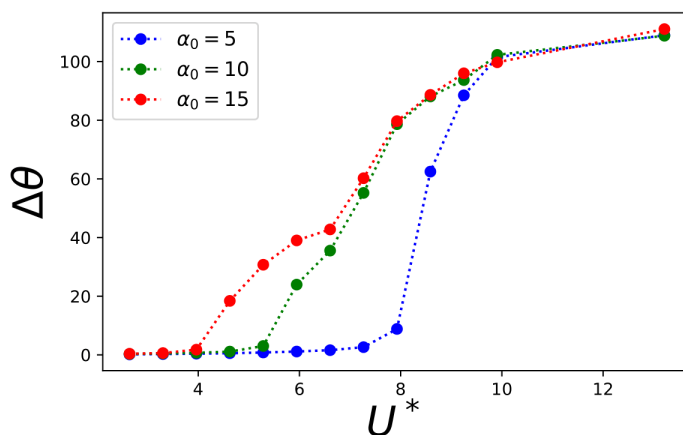


Figure 5. Oscillation amplitude (in degrees) v/s reduced velocity at $Re = 1000$, for three different values of equilibrium angle-of-attack (α_0).

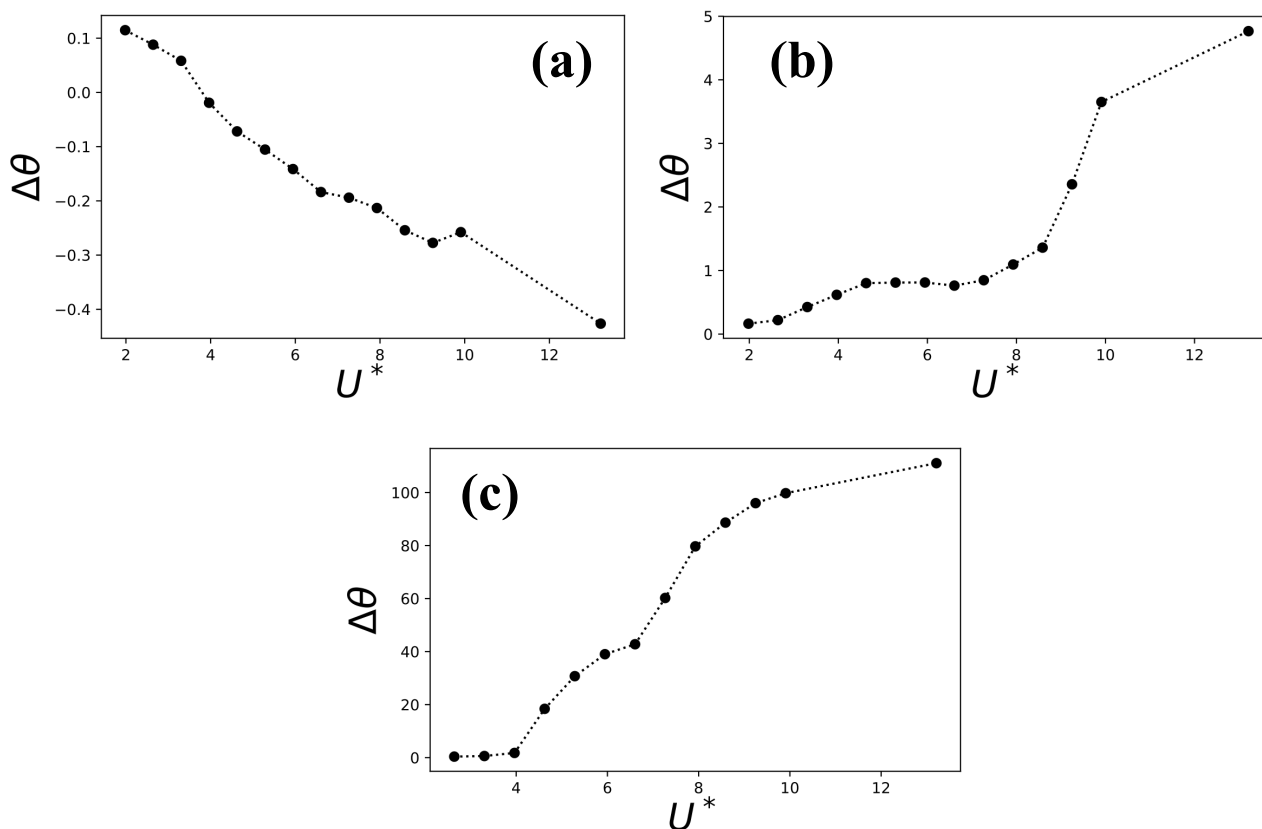


Figure 6. Pitching amplitude (in degrees) v/s reduced velocity for different values of hinge location for $\alpha_0 = 15^\circ$: (a) $X_h = 0.25$; (b) $X_h = 0.33$; (c) $X_h = 0.50$.

Figure 5 shows a plot of maximum pitching amplitude as a function of U^* for three different equilibrium angles-of-attack. The equilibrium angle-of-attack corresponds to α_0 in the dynamical equation of motion for the system. It is

seen that for higher equilibrium angles-of-attack, the system is unstable at lower values of U^* . Additionally, even though higher values of U^* are required to trigger the flutter instability at low equilibrium angles-of-attack, we see that the amplitude seems to saturate at high U^* , with the system effectively losing memory of the equilibrium angle-of-attack. It is also seen that the system is capable of exhibiting very large amplitude oscillations, going as high as 100° for the values of U^* simulated in this study.

C. Effect of Elastic Axis Location

In Figure 2, the plot of center-of-pressure v/s angle-of-attack for the static airfoil showed that the center-of-pressure varied roughly between $0.25C$ and $0.4C$ for the angles-of-attack studied. This suggests that locating the elastic axis aft of $0.4C$ would result in an unstable system, since an increase in angle-of-attack, and hence lift, would result in a higher pitching moment by virtue of the upstream location of the center-of-pressure. On the other hand, locating the elastic axis upstream of the center-of-pressure will have the opposite effect on pitching moment, thus stabilizing the system. However, it is not clear that this simplistic picture explains the situation of a dynamically pitching airfoil. In Figure 6 we show the pitching amplitude response of the airfoil, with $\alpha_0 = 15^\circ$, for three different locations of the elastic axis. It is seen that if $X_h = 0.25$, the airfoil is significantly stabilized as compared to $X_h = 0.50$. The pitching amplitudes for the former are two orders-of-magnitude smaller than those for the latter. Overall, we see from Figure 6 that small changes in the location of the elastic axis – from $0.25C$ to $0.33C$, as well as $0.33C$ to $0.5C$ – lead to the pitch amplitude changing by orders of magnitude. This points to the inherent nonlinearity of the coupled system and the sensitivity to parameters, even in the presence of a simplified and linear structural model.

D. Force Partitioning Method

We now present a recently developed method for decomposing the forces on an immersed body [15] into components that are readily identified with distinct physical mechanisms in the flow. The goal here is use this partitioning to generate insights into the physical mechanism that drive the dynamics of such aeroelastic systems. In many areas of fluid dynamics, and particularly in problems involving fluid-structure interactions, the ability to delineate the physical origin of the various forces acting on the body, and hence the forcing mechanism, can prove invaluable in better understanding and/or controlling the system under question. In general, the force due to the fluid on an immersed body in the i direction is given by,

$$\vec{F}_B^{(i)} = \int_B (p\hat{n}_i + \vec{\tau}_w^{(i)}) dS$$

where \hat{n} is the unit vector on the surface of the immersed body, B is the surface of the body, and (i) denotes the direction of the force of interest. The pressure force on the body might however be attributable to different mechanisms such as vortex-induced force, added-mass, viscous diffusion and others. A number of methods have been proposed in the past to decompose the fluid force on a body into distinct components, and the method proposed here is based on the force projection method of Quarterpelle and Napolitano [16]. The essence of the method is the definition of a scalar potential, defined as:

$$\nabla^2 \phi^{(i)} = 0; \hat{n} \cdot \nabla \phi^{(i)} = \begin{cases} n_i & \text{on } B \\ 0 & \text{on } \Sigma \end{cases}$$

where Σ is the outer boundary of the computational domain and n_i is the component of the unit normal in the (i) direction. The incompressible Navier-Stokes momentum equation are then projected on to the gradient of this scalar field, and subsequently integrated over the volume of the domain, as follows:

$$\int_v \frac{\partial \vec{u}}{\partial t} \cdot \nabla \phi^{(i)} + \int_v \nabla \cdot (\vec{u}\vec{u}) \cdot \nabla \phi^{(i)} = \int_v -\nabla p \cdot \nabla \phi^{(i)} + \int_v \left(\frac{1}{Re}\right) \nabla^2 \vec{u} \cdot \nabla \phi^{(i)}$$

Going further, we utilize Helmholtz decomposition to divide the velocity field into a potential flow and vortical flow component, $\vec{u} = \vec{u}_v + \vec{u}_\phi$. Subsequent mathematical manipulations [15] then lead to the following expressions for the various force components on the body:

$$F_k^{(i)} = -\rho \int_B \vec{n} \cdot \frac{d\vec{U}}{dt} \phi^{(i)} dS - \frac{1}{2} \rho \int_B U^2 n_i dS$$

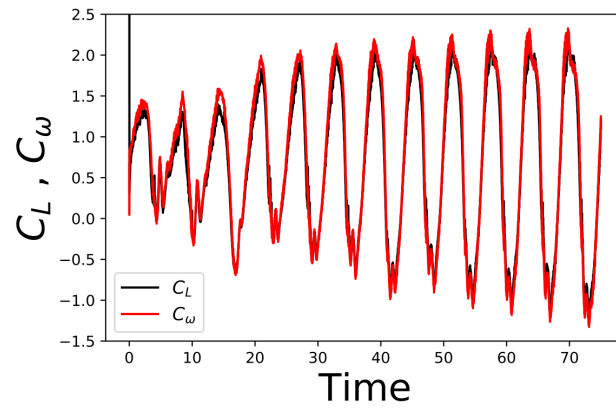


Figure 7. Timeseries of total and vortex-induced lift coefficients on a pitching airfoil, for $\alpha_0 = 15$ and $U^* = 6.6$.

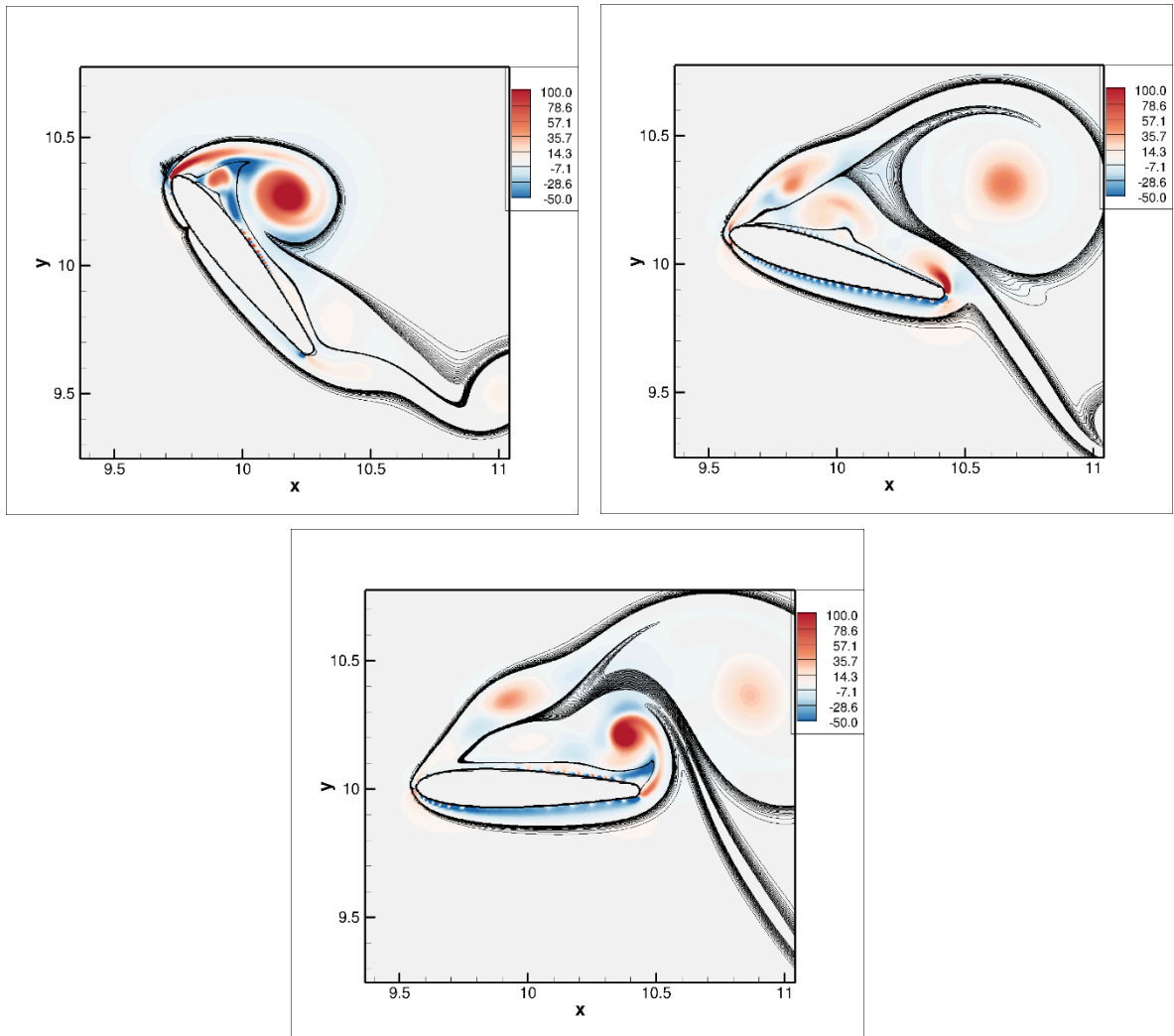


Figure 8. Contour plot of vortex-induced lift coefficient per unit fluid volume, for a pitching airfoil at $\alpha_0 = 15$ and $U^* = 6.6$. Red and blue contours indicate positive and negative lift contribution respectively. The superposed contour lines correspond to the z-component of vorticity.

$$\begin{aligned}
F_{\omega}^{(i)} &= \rho \int_{V_f} \nabla \cdot \left[\nabla \left(\vec{u}_v \cdot \vec{u}_\phi + \frac{1}{2} \vec{u}_v \cdot \vec{u}_v \right) \phi^{(i)} \right] dV + \rho \int_{V_f} [\nabla \cdot (\vec{\omega} \times \vec{u})] \phi^{(i)} dV \\
F_{\phi}^{(i)} &= \rho \int_B \vec{n} \cdot \left(\nabla \left(\frac{1}{2} u_\phi^2 \right) \phi^{(i)} \right) dS \\
F_{\sigma}^{(i)} &= \mu \int_B (\vec{\omega} \times \vec{n}) \cdot \nabla (\phi^{(i)} - x_i) dS
\end{aligned}$$

where $F_{\kappa}^{(i)}$, $F_{\omega}^{(i)}$, $F_{\phi}^{(i)}$, and $F_{\sigma}^{(i)}$ are respectively kinematic, vortex-induced, potential-flow, and viscous forces on the body in the i direction. A particularly valuable aspect of this force decomposition tool is that it allows us to isolate the individual contributions of each vortex in the flow field to the total force on the body. This comes from the fact that the vortex induced force is a volume integral, as shown in the above equation for \vec{F}_{ω} . Hence, by limiting the volume of integration, we can delineate the contribution any chosen flow structure. This is a powerful way to analyze the influence of the complicated wake structures seen in the representative snapshots of the flow in Figure 4.

As a demonstration of this method, we show a sample case of a simulation with $\alpha_0 = 15^\circ$ and $U^* = 6.6$. We have confirmed (not shown here) that the contributions from the kinematic and shear force, F_{κ} and F_{σ} respectively, are orders of magnitude smaller, hence the dynamics is primarily driven by vortex shedding. Figure 7 shows a timeseries of vortex-induced lift coefficient, $C_{\omega} = F_{\omega} / (\frac{1}{2} \rho U_{\infty}^2 C)$, compared with a timeseries of total lift coefficient. We see that C_{ω} accounts for nearly all the lift. In Figure 8 we show snapshots of the flow, coloured by local contributions of C_{ω} per unit volume. Here, contours coloured in red represent positive lift production. The large contribution of the LEV is evident from these figures, as is the positive contribution of the other vortices shed over the suction surface of the airfoil over the course of the oscillation cycle. It is also seen that the effect of each vortex diminishes with distance from the airfoil, as expected. Interestingly, while the core of the LEV is seen to contribute to positive lift, it is embedded in a region of vorticity that generates negative lift. It must be noted, however, that the net lift at this stage is positive. The exact contribution of different parts of the flow-field to the lift are yet to be investigated and is a subject of ongoing work.

IV. Conclusions

Computational simulations of flow-induced pitching oscillations of a NACA0015 airfoil have been carried out at $Re = 1000$. A parametric study of pitching response as a function of equilibrium angle-of-attack, reduced velocity, and location of elastic axis is reported on. It is seen that increasing the equilibrium angle-of-attack reduces the critical U^* at which the system becomes unstable to angular perturbations. Further, the system loses memory of the equilibrium angle-of-attack for large amplitude oscillations. A study of the system's sensitivity to the location of the elastic axis showed results that were largely in line with the static airfoil stability predictions. Further, a force partitioning tool was applied to a sample case of a pitching airfoil and it indicates the ability to dissect the contribution of various vortices to the aerodynamic forces on the airfoil.

Acknowledgments

This work is supported by AFOSR Grant FA9550-16-1-0404, monitored by Dr. Douglas Smith.

References

- [1] L. E. Ericsson and J. P. Reding, "Fluid mechanics of dynamic stall part I. Unsteady flow concepts," *J. Fluids Struct.*, vol. 2, no. 1, pp. 1–33, 1988.
- [2] W. J. McCroskey, "Unsteady Airfoils," *Ann. Rev. Fluid Mech.*, vol. 14, pp. 285–311, 1982.
- [3] T. Lee and P. Gerontakos, "Investigation of flow over an oscillating airfoil," *J. Fluid Mech.*, vol. 512, pp. 313–341, 2004.
- [4] M. R. Amiralaee, H. Alighanbari, and S. M. Hashemi, "An investigation into the effects of unsteady parameters on the aerodynamics of a low Reynolds number pitching airfoil," *J. Fluids Struct.*, vol. 26, no. 6, pp. 979–993, 2010.
- [5] A. H. Lind and A. R. Jones, "Unsteady aerodynamics of reverse flow dynamic stall on an oscillating blade section," *Phys. Fluids*, vol. 28, no. 7, 2016.

- [6] J. Young and J. C. S. Lai, "Oscillation Frequency and Amplitude Effects on Plunging Airfoil Propulsion and Flow Periodicity," *AIAA J.*, vol. 42, no. 10, pp. 2042–2052, 2004.
- [7] S. S. Bhat and R. N. Govardhan, "Stall flutter of NACA 0012 airfoil at low Reynolds numbers," *J. Fluids Struct.*, vol. 41, pp. 166–174, 2013.
- [8] G. Dimitriadis and J. Li, "Bifurcation Behavior of Airfoil Undergoing Stall Flutter Oscillations in Low-Speed Wind Tunnel," *AIAA J.*, vol. 47, no. 11, pp. 2577–2596, 2009.
- [9] A. Ducoin and Y. L. Young, "Hydroelastic response and stability of a hydrofoil in viscous flow," *J. Fluids Struct.*, vol. 38, pp. 40–57, 2013.
- [10] E. H. Dowell, "Nonlinear Oscillations of a Fluttering Plate," *AIAA J.*, vol. 4, no. 7, pp. 1267–1275, 1966.
- [11] P. Holmes and J. Marsden, "Bifurcation to divergence and flutter in flow-induced oscillations: an infinite dimensional analysis," *Automatica*, vol. 14, no. 4, pp. 367–384, 1978.
- [12] E. J. Jumper, R. L. Dimmick, and A. J. S. Allaire, "The effect of pitch location on dynamic stall," *J. Fluids Eng.*, vol. 111, no. 3, pp. 256–262, 1989.
- [13] R. Mittal, H. Dong, M. Bozkurtas, F. M. Najjar, A. Vargas, and A. von Loebbecke, "A versatile sharp interface immersed boundary method for incompressible flows with complex boundaries," *J. Comput. Phys.*, vol. 227, no. 10, pp. 4825–4852, 2008.
- [14] J. H. Seo and R. Mittal, "A sharp-interface immersed boundary method with improved mass conservation and reduced spurious pressure oscillations," *J. Comput. Phys.*, vol. 230, no. 19, pp. 7347–7363, Aug. 2011.
- [15] C. Zhang, T. L. Hedrick, and R. Mittal, "Centripetal acceleration reaction: An effective and robust mechanism for flapping flight in insects," *PLoS One*, vol. 10, no. 8, pp. 1–16, 2015.
- [16] L. Quartappelle and M. Napolitano, "Force and moment in incompressible flows," *AIAA J.*, vol. 21, no. 6, pp. 911–913, 1982.